Finite Element Simulation of Metal–Semiconductor–Metal Photodetector

Introduction

Low-temperature–grown GaAs (LT-GaAs), deposited by molecular beam epitaxy, has been known for its ultrashort, subpicosecond photocarrier lifetime and relatively high carrier mobility. Therefore, in recent years LT-GaAs has been the material of choice for the fabrication of photonic devices such as photoconductive switches,[1,2] both of the metal–semiconductor–metal (MSM)[3] and freestanding types,[4] for the generation of subpicosecond electrical pulses for ultrafast device characterization,[5] THz time-domain spectroscopy,[6] antennas for the generation and detection of THz radiation,[7] as well as for optical photomixers.[8,9]

Much effort has gone into achieving high efficiency for LT-GaAs material and the design of optimal geometries for the device structures; however, further performance improvement of LT-GaAs–based photonic devices is expected by optimizing the device contacts. Historically, LT-GaAs MSM's have been constructed with electrodes consisting of surface-contact metallization such as, e.g., Ni-Au, Ti-Au, or Ti-Pd-Au.[10] For decades the properties of metal contacts to III–V semiconductors have been intensively studied.[11,12] From these studies it is well known that a contact metallization that creates Schottky contacts on conventional *n*-doped GaAs shows ohmic behavior on LT-GaAs, even without annealing.[10] The annealing of contacts to LT-GaAs is restricted to temperatures below 600°C since higher temperatures lead to a drastic change in the properties of the LT-GaAs material itself. The speed of response for the ohmic-type MSM photodetector is generally limited by the carrier lifetime, which in the case of LT-GaAs is so short (~150 fs) that the device capacitance sets the practical limit. Unfortunately, the ultrashort carrier lifetime translates into relatively low mobility of the LT-GaAs material, resulting in low-efficiency LT-GaAs devices, as compared to other photodetectors, such as *p-i-n* diodes.[13] Recently, however, MSM devices with alloyed[12,14] and recessed[9,15] electrodes have been found to exhibit improved performance through optimization of the device contacts. Reference 14 reported a twofold improvement in efficiency using alloyed contacts based on Au-Ge eutectic, and Ref. 15 reported a 25% increase in sensitivity using recessed surface contacts.

This article presents a finite element model to analyze the photoresponse of two types of LT-GaAs MSM's, both of the same device geometry, but one with non-alloyed surface contacts and the other with alloyed contacts. Based on experimental work,[14] the simulated photodetectors consist of interdigitated conductors, patterned on a 1.5-μm-thick LT-GaAs layer, grown by molecular beam epitaxy at 250°C, followed by *in-situ* isothermal annealing at 600°C. We can, therefore, directly correlate our simulations with the experimental results and understand the physical reasons for the improved photoresponse efficiency of the alloyed-contact LT-GaAs MSM's without sacrificing the response times. We demonstrate that indeed the latter devices have better-than-twice the sensitivity of the surface-contact structures and better-than-50% improvement in response time. We further use our model to propose the configuration of optimized devices.

Finite Element Model

The finite element simulations presented here were created with the COMSOL Multiphysics® Finite Element Analysis (FEA) software package[16] using the generalized electrostatics mode. In this mode, the equation of continuity is combined with Gauss's law, and the partial differential equation to be solved is

$$-\nabla \cdot \left[\left(\sigma + \varepsilon_0 \varepsilon_r / T\right) \nabla V - \mathbf{J}^{\mathrm{e}}\right] = \rho_0 / T, \tag{1}$$

where σ and $\varepsilon_r \varepsilon_0$ are the material's conductivity and permittivity, respectively, V is the electric potential, $\mathbf{J}^{\mathrm{e}}$ is an externally sourced current density, ρ_0 is the given space-charge density at $t = 0$, and T is a time constant chosen to be large relative to the maximum charge relaxation time of the system. For the simulations presented here, $\mathbf{J}^{\mathrm{e}}$ and ρ_0 are set to zero and T was chosen to be 10^{-2} s. Increasing T above 10^{-2} s had no effect on the results; making it too large, however, could result in an ill-conditioned FEA formulation.

The model geometry is a two-dimensional cross section of one of the photoconductive LT-GaAs channels plus the electrodes. The results of the simulation are given per meter, and the result is multiplied by the overall length of the channel, which is 147 μm. Figure 119.36 shows a schematic of the MSM top view and cross section used for simulation. The model boundary condition is electrical insulation everywhere, except for the small spans, where the electrode intersects the boundary and the condition is a fixed electrical potential. The actual fabricated device[14] had an area of 400 μm^2 and an electrode finger width and spacing of 1 μm and 1.5 μm, respectively. The alloyed-electrode MSM consisted of a Ni-Au/Ge-Ni-Au layer stack with 5-, 90-, 25-, and 50-nm thickness, respectively, alloyed at 420°C for 90 s. The surface-contact device had a Ni-Au layer with a thickness of 10 to 160 nm.

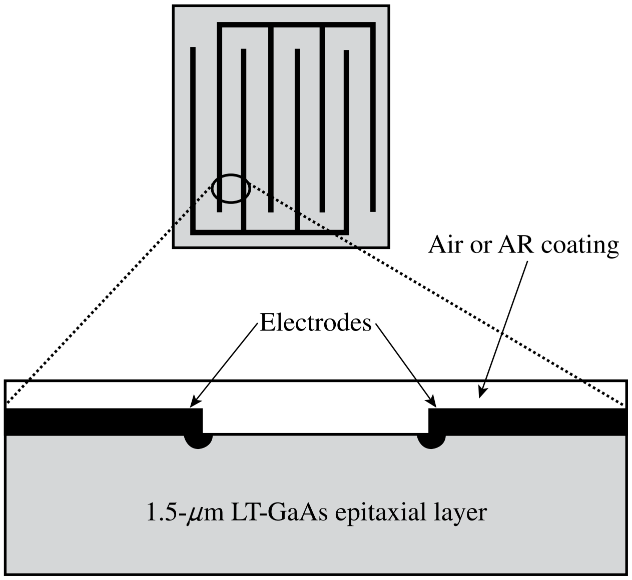

E17561JR

Figure 119.36
Schematic top view of an MSM device and side view of one photoconductive channel, with electrodes on each side.

Figures 119.37 and 119.38 show arrow plots of the electric field and current density, created with COMSOL Multiphysics®. The simulation results in Fig. 119.37 are for the alloyed-electrode device, illuminated by 850-nm-wavelength light, with a nominal alloy depth of L = 200 nm. The simulation results in Fig. 119.38 are for the surface-contact device, with identical illumination conditions. The length of the arrows is scaled according to the magnitude of the quantity they represent. We note in Fig. 119.37 that for the alloyed device, the electric field is uniformly distributed in the photoconductive region, and the current density in this region decays as does the intensity of the incident light. On the other hand, the surface contact device in Fig. 119.38 shows a very different electric field distribution, and the current is channeled entirely through the corner insets of the electrodes.

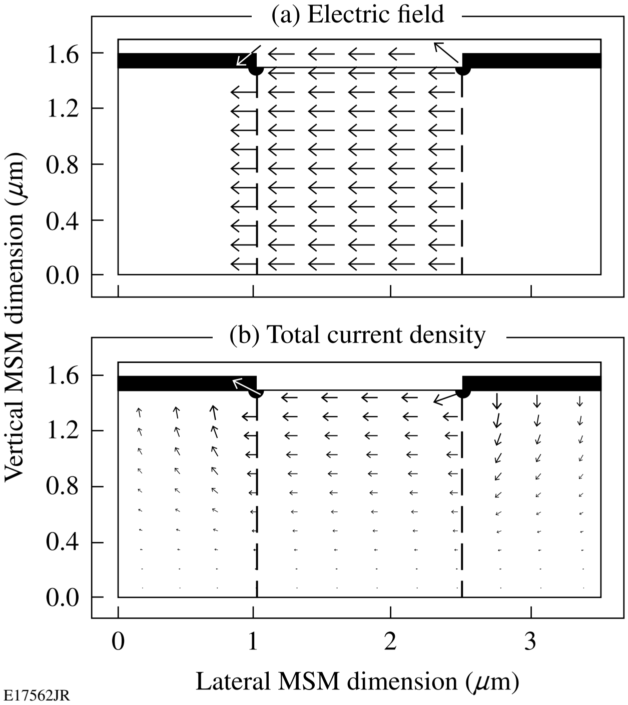

E17562JR

Figure 119.37
Arrow plots of the (a) electric field and (b) current density for the alloyed-contact device with L = 200 nm. These plots were created using COMSOL Multiphysics®.[16]

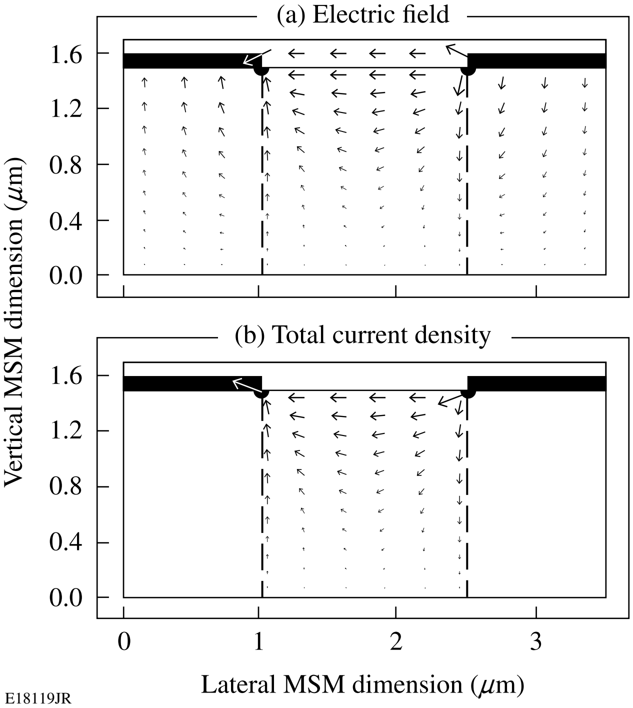

E18119JR

Figure 119.38
Arrow plots of the (a) electric field and (b) current density for the surface-contact device. These plots were created using COMSOL Multiphysics®.[16]

For the FEA model, each device was divided into five subdomains, consisting of the two electrodes, the photoconductive region, and the two LT-GaAs regions under the electrodes. For simplicity, the two electrodes were assigned a conductivity $\sigma = 45.6 \times 10^6$ S/m, typical for Au. The conductivity profile of the photoconductive region was calculated based on illumination with 160 μW of continuous-wave light, consistent with the experimental setup in Ref. 14. The transmission coefficient was calculated as 43%, based on the LT-GaAs refractive index of 3.64 at 850 nm (Ref. 17), and the internal quantum efficiency (QE) was taken as 1. These factors, in addition to 40% loss of input power as a result of the reflectivity of the metal electrodes, give $G = 1.77 \times 10^{14}\ \mathrm{s}^{-1}$, the overall (volume) carrier-generation rate. By assuming that the carrier generation decays in the same manner as incident 850-nm light with a penetration depth $l = 1\ \mu$m, and integrating over the photoconductive volume, the carrier generation at the surface was calculated to be $G_\mathrm{S} = 9.47 \times 10^{23}\ (\mathrm{s} \bullet \mathrm{cm}^3)^{-1}$.

To relate G_S to σ, it is necessary to compute the resulting steady-state carrier density. This was done by setting the generation equal to the Shockley–Read–Hall recombination rate, simplified by assuming that the recombination centers are located at the bandgap. The electron and hole concentrations at the surface, n_s and p_s, respectively, can then be calculated as

$$n_\mathrm{s} = p_\mathrm{s} = n_\mathrm{i} + 2 \cdot G_\mathrm{S} \cdot \tau, \tag{2}$$

where n_i is the intrinsic GaAs carrier concentration and τ is the carrier lifetime. Taking for LT-GaAs at 300 K, $n_\mathrm{i} = 1.8 \times 10^6\ \mathrm{cm}^{-3}$, $\tau = 150$ fs (Ref. 5), and the mobility for photogenerated carriers to be $\mu \approx 200\ \mathrm{cm}^2/(\mathrm{V} \bullet \mathrm{s})$ (Ref. 1), we may then compute the surface conductivity $\sigma_\mathrm{s} = 2n_\mathrm{s}\mu = 1.8$ mS/m, and, subsequently, the conductivity profile

$$\sigma = \sigma_\mathrm{s} \cdot \exp\left(\frac{-z}{l}\right), \tag{3}$$

where z is the distance from the LT-GaAs surface.

So far everything said about our MSM FEA model applies to both the alloyed and non-alloyed devices. The difference between the two is the conductivity profile under the contacts. In the case of the non-alloyed device, the conductivity of the region under the contact is simply that of LT-GaAs, which is essentially an insulator. In the case of the alloyed device, a Ni-AuGe-Ni-Au layer stack forms the electrode. Subsequent alloying at 420°C for 90 s causes Ge atoms to migrate into the LT-GaAs, with an expected penetration depth of $L = 200$ nm (Ref. 18). As a result, the conductivity at the interface between the contact metallization and the alloyed LT-GaAs is that of Ge and decays exponentially to the conductivity of LT-GaAs under the contact. The σ profile under the alloyed contact is therefore

$$\sigma_\mathrm{ac} = \left(\sigma_\mathrm{Ge} - \sigma_\mathrm{LT}\right) \cdot \exp\left(\frac{-z}{L}\right) + \sigma_\mathrm{LT}, \tag{4}$$

where $\sigma_\mathrm{Ge} = 2.2$ S/m and $\sigma_\mathrm{LT} = 1.15 \times 10^{-8}$ S/m are the conductivities of Ge and LT-GaAs, respectively.

One additional feature that requires some explanation is the semicircular inset at the inside corner of each electrode shown in Fig. 119.36. In the case of the alloyed-contact MSM, this feature has no effect on results; it is, however, essential for modeling the surface-electrode device since without it there would be no lateral path for current. Figure 119.36 is not to scale and the corner insets are exaggerated for clarity. The actual radius used in our modeling was only 50 nm, based on the simple estimation that the carriers generated near the edge of the surface electrode may drift/diffuse into the insulating region toward the electrode on the scale of the carrier mean free path, equal in our case to ~66 nm, for a Fermi velocity of 4.4×10^5 m/s (Ref. 12) and $\tau = 150$ fs. A change of ±50% in this radius did not impact results of the model.

Results

1. Responsivity

For the alloyed-contact device, the responsivity predicted by the model was 8.6×10^{-4} A/W, while the actual measured value in Ref. 14 was 13.7×10^{-4} A/W. For the surface-electrode MSM, the corresponding simulation and experimental values were 3.7×10^{-4} A/W and 6.2×10^{-4} A/W, respectively. Considering the approximations involved, the results of the FEA model can be considered reasonably close to measured. The responsivity is dependent on μ, quantum efficiency, transmission coefficient of LT-GaAs, alloy depth, and the contact resistance. If we, for example, used a carrier mobility of only $\mu \approx 320\ \mathrm{cm}^2/(\mathrm{V} \bullet \mathrm{s})$, instead of $200\ \mathrm{cm}^2/(\mathrm{V} \bullet \mathrm{s})$, we would get full agreement between our model and the experiment. We note here that although the relatively low values of μ for LT-GaAs have been well documented,[8] some sources have reported μ's as high as $2000\ \mathrm{cm}^2/(\mathrm{V} \bullet \mathrm{s})$ (Refs. 19 and 20), depending on the sample processing. For QE the range of numbers in the literature spans from 1 (Ref. 21) to 0.07 (Ref. 5). We assumed the ideal case of QE = 1. Our transmission coefficient was calculated to be 43%, based on the refractive index of GaAs at

850 nm, and, finally, the depth of alloying under the contacts was taken to be 200 nm based on the expected (but not measured) depth stated in Ref. 14.

In view of the above, the responsivity ratio of MSM's with alloyed to non-alloyed contacts is of particular interest. The FEA model yielded a ratio of 2.3, while the experimental value in Ref. 14 was 2.2. Therefore, we may conclude that our model does a good job of predicting the improvement in responsivity obtained using photodetectors with alloyed contacts.

2. Capacitance and Transient Response

Typically, photoconductive devices turn on much faster than they turn off since the rising part of the photoresponse limits how fast optical energy is delivered to the photocarriers and simply corresponds to the integral of the optical-pulse intensity. The turn-off time, on the other hand, depends on the mechanism of carrier sweep (Schottky type) or on the carrier lifetime in the photoconductive region. In the case of LT-GaAs devices exhibiting ohmic contacts, the latter is true; however, since τ is in the femtosecond range, the actual device turn-off time is limited by stored charge and the equivalent lumped-element resistive-capacitive (RC) time constant.

Table 119.IV shows the capacitance of the alloyed- and surface-electrode devices in both the light-ON and light-OFF states, as predicted by the FEA model. The higher capacitance of the alloyed-contact MSM is expected from the device configuration and suggests that its photoresponse signal should be slower. However, the photoresponse measurements performed in Ref. 14 actually indicate that alloyed devices exhibit somewhat faster turn-offs, while in both cases, the turn-on time is about the same. The photoresponse transients in Ref. 14 show a turn-off time constant of the alloyed device to be 1.8 ps and 2.8 ps for the non-alloyed structure. In terms of our model, an improvement of the turn-off time in the alloyed-electrode MSM's can be understood if one considers the accumulated charge at the boundary between the LT-GaAs photoconductive region and either the alloyed or non-alloyed region under the electrode surface. In the ON state, both devices have a significant charge, accumulated at this boundary. In the case of the surface-contact MSM, however, this boundary effectively goes away when the device turns off, leaving the charge to dissipate through the volume of the very highly resistive LT-GaAs. On the other hand, in the alloyed-contact MSM case, the relatively high conductance of the alloyed-contact volume makes possible a much more efficient discharge of the equivalent capacitor. Based on the ratio of sensitivities of the two devices, the effective ON-state resistance of the alloyed device is 2.2× lower than that of the non-alloyed device. Thus, including the capacitances listed in Table 119.IV, the ratio of the corresponding RC time constants is 1.47 and should be the same as the ratio of the fall times of the respective photoresponse transients. Note that the experimentally measured ratio in Ref. 14 is 1.56, in excellent agreement with the prediction of our model. As a result, despite the larger geometrical capacitance, the alloyed-contact MSM is actually faster than the surface-electrode structure, as indeed was experimentally observed.

Table 1119.IV: MSM device capacitance in the OFF and ON states, with or without an AR coating.

	Surface contact	Alloyed contact
OFF, no AR	10.2 (fF)	17.0 (fF)
OFF, with AR	10.7 (fF)	17.5 (fF)
ON, no AR	10.4 (fF)	15.6 (fF)
ON, with AR	10.5 (fF)	16.0 (fF)

3. Device Optimization

The results of the FEA model are well correlated to experimental values; therefore, the model may be used to predict the effect of various parameters on MSM photoresponse performance. In this section, we look at how such technological parameters as the depth of the alloyed contacts, electrode spacing, or additional antireflection (AR) coating, influence the device's performance.

Figure 119.39 shows the responsivity as a function of alloy penetration depth L, which is the exponential spatial decay constant of σ under the alloyed contact [see Eq. (4)]. As the L

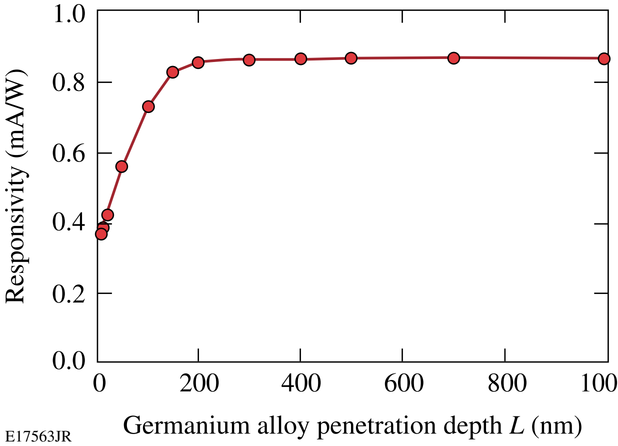

Figure 119.39
Responsivity versus the alloy penetration depth for an alloyed-contact MSM.

value decreases to zero, approximating the surface-type contact, the point where the responsivity curve intersects the y axis approaches the responsivity of the surface-electrode MSM. We observe in Fig. 119.39 that for $L > 200$ nm the curve flattens, so increasing L beyond 200 nm results in very little improvement. The latter is fully understandable looking at Fig. 119.37(a) and noting that at $L = 200$ nm the electric field is already fairly uniform down through the photoconductive region. The electric potential between the boundaries of the photoconductive region is also uniform and equal to the applied electrode potential, so current is strictly limited by the photoconductance.

Figure 119.40 shows the responsivity as a function of electrode spacing, for both an alloyed- and a surface-contact MSM. For the alloyed device, the relationship can be easily and precisely explained because the resistance of the photoconductive channel is proportional to its length. Therefore, the responsivity is proportional to current and, consequently, inversely proportional to the channel length. For the surface-electrode MSM, the relationship is not as simple due to the concentration of current at the corner insets of the electrodes, as seen in Fig. 119.38. The corner insert will come into play only when the spacing approximately equals the radius. As the spacing decreases for the surface-electrode device, the electric field gets pulled toward the surface. Therefore, carriers generated far below the surface do not contribute to the sensitivity.

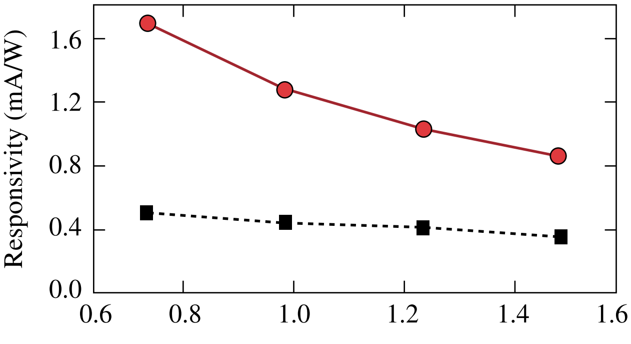

Figure 119.40
Responsivity versus the electrode finger spacing for an alloyed-contact (solid line) and surface-contact (dashed) MSM.

Finally, our FEA model predicts that an AR coating should obviously improve the device responsivity by decreasing the amount of reflected light, but, at the same time, the additional dielectric material deposited on top of the photodetector increases its capacitance. We observe a typical trade-off between the responsivity and speed. However, in the case of the alloyed-contact structures our simulations show (see Table 119.IV) that the actual increase in the capacitance is less than 5%. As a result, a well-designed AR coating in such structures clearly leads to an overall improvement in the photodetector's performance by increasing the responsivity without significant degradation in speed.

Conclusion

A simple FEA model, using the COMSOL Multiphysics® software package,[16] has been developed to simulate the photoresponse of the MSM photodetector. The two experimentally most-viable cases, namely devices with either alloyed- or non-alloyed-surface contacts, have been studied and have demonstrated that in both cases, both the photodetector responsivity and the time-domain response can be very accurately simulated. This approach also allows one to optimize the MSM design, indicating that deposition on the photodetector surface of an AR coating, while substantially increasing its responsivity, only marginally affects the photoresponse time constant.

ACKNOWLEDGMENT

This work is supported by the NSF NIRT Grant No. ECS-0609140. Additional support was provided by the U.S. Department of Energy Office of Inertial Confinement Fusion under Cooperative Agreement No. DE-FC52-08NA28302, the University of Rochester, and the New York State Energy Research and Development Authority. The support of DOE does not constitute an endorsement by DOE of the views expressed in this article.

REFERENCES

1. F. W. Smith, in *Low Temperature (LT) GaAs and Related Materials*, edited by G. L. Witt *et al.*, Mat. Res. Soc. Symp. Proc. Vol. 241 (Materials Research Society, Pittsburgh, PA, 1992), pp. 3–12.
2. S. Gupta, J. F. Whitaker, and G. A. Mourou, IEEE J. Quantum Electron. **28**, 2464 (1992).
3. S. Y. Chou, Y. Liu, and W. Khalil, Appl. Phys. Lett. **61**, 819 (1992).
4. M. Marso, M. Mikulics, R. Adam, S. Wu, X. Zheng, I. Camara, F. Siebe, A. Forster, R. Gusten, P. Kordoš, and R. Sobolewski, Acta Phys. Pol. A **107**, 109 (2005).
5. X. Zheng, Y. Xu, R. Sobolewski, R. Adam, M. Mikulics, M. Siegel, and P. Kordoš, Appl. Opt. **42**, 1726 (2003).
6. S. Kono *et al.*, Appl. Phys. Lett. **77**, 4104 (2000).
7. X.-C. Zhang, J. Lumin. **66 & 67**, 488 (1996).
8. S. Verghese, K. A. McIntosh, and E. R. Brown, Appl. Phys. Lett. **71**, 2743 (1997).
9. M. Mikulics *et al.*, Appl. Phys. Lett. **88**, 041118 (2006).

10. H. Yamamoto, Z-Q. Fang, and D. C. Look, Appl. Phys. Lett. **57**, 1537 (1990).

11. N. Braslau, J. B. Gunn, and J. L. Staples, Solid State Commun. **10**, 381 (1967).

12. N. Vieweg *et al.*, Opt. Express **16**, 19,695 (2008).

13. S. Collin, F. Pardo, and J.-L. Pelouard, Appl. Phys. Lett. **83**, 1521 (2003).

14. M. Mikulics, M. Marso, S. Wu, A. Fox, M. Lepsa, D. Grützmacher, R. Sobolewski, and P. Kordoš, IEEE Photon. Technol. Lett. **20**, 1054 (2008).

15. M. Mikulics, S. Wu, M. Marso, R. Adam, A. Förster, A. van der Hart, P. Kordoš, H. Lüth, and R. Sobolewski, IEEE Photonics Technol. Lett. **18**, 820 (2006).

16. COMSOL® and COMSOL Multiphysics® are registered trademarks of COMSOL AB, Tegnérgatan 23, SE-111 40 Stockholm, Sweden.

17. J. S. Blakemore, J. Appl. Phys. **53**, R123 (1982).

18. M. Ogawa, J. Appl. Phys. **51**, 406 (1980).

19. K. Xie and C. R. Wie, in *Low Temperature (LT) GaAs and Related Materials Symposium*, edited by G. L. Witt *et al.*, Mat. Res. Soc. Symp. Proc. Vol. 241 (Materials Research Society, Pittsburgh, PA, 1992), pp. 33–38.

20. A. C. Warren *et al.*, in *Low Temperature (LT) GaAs and Related Materials Symposium*, edited by G. L. Witt *et al.*, Mat. Res. Soc. Symp. Proc. Vol. 241 (Materials Research Society, Pittsburgh, PA, 1992), pp. 15–25.

21. Electrical Properties of Gallium Arsenide, IOFFE-Physico Technical Institute, St. Petersburg 194021, Russia, http://www.ioffe.ru/SVA/NSM/Semicond/GaAs/electrical.html.